JM PAPERS

Turbulent wake characteristics for a circular cylinder in proximity to a moving wall

Hongyi Jiang[1,2], Xiaoying Ju[3],†, Zhen Guo[2] and Lizhong Wang[2]

[1]Ocean College, Zhejiang University, Zhoushan 316021, PR China

[2]Key Laboratory of Offshore Geotechnics and Material of Zhejiang Province, Zhejiang University, Hangzhou 310058, PR China

[3]School of Marine Engineering Equipment, Zhejiang Ocean University, Zhoushan 316022, PR China

This study investigates the scenario of flow past a circular cylinder in proximity to a moving wall (or equally a body translating in still fluid parallel to a stationary wall). Fifty high-fidelity three-dimensional direct numerical simulations are performed over a parameter space of turbulent Reynolds numbers (Re) of 300 to 1000 combined with gap-to-diameter ratios (G/D) of 0.2 to 3. The flow, hydrodynamic and turbulence characteristics over the (Re, G/D) parameter space are examined in detail. Small-scale rib-like mode B structures and alternate vortex shedding are observed for all cases. The streamwise location for the vortex shedding (quantified by the wake recirculation length L_r) varies strongly with both Re and G/D. The variation of L_r with Re and G/D can be explained by the spanwise circulation Γ_z fed into the wake, where the variation trends of L_r and Γ_z are inversely correlated. The variations of the mean drag and fluctuating lift coefficients are also governed by the variations in L_r and Γ_z. The total kinetic energy in the wake region reduces drastically as G/D reduces below 0.8, which is contributed collectively by (i) reduction in the strength of the shed vortices, (ii) downstream movement of the location of vortex shedding and (iii) associated delayed generation of streamwise vortices. The present results on a moving wall also help to explain several flow and hydrodynamic characteristics reported in the literature for a stationary wall, because the moving wall eliminates the complex wall boundary layer and retains a 'clean' near-wall effect.

Key words: vortex shedding, wakes

1. Introduction

The scenario of steady uniform approaching flow past a smooth and slender circular cylinder is a classical fluid mechanics problem with both fundamental and

† Email address for correspondence: xiaoying.ju@outlook.com

practical significance. For this scenario, the sole governing parameter is the Reynolds number Re $(= UD/\nu)$, which is defined based on the free stream velocity U, diameter of the cylinder D and kinematic viscosity of the fluid ν. With the increase in Re, several flow regimes/transitions have been observed, which include onset of vortex shedding, onset of three-dimensionality, transition to chaos, successive transitions to turbulence in the wake, the separating shear layer and the boundary layer (see e.g. Williamson 1996; Zdravkovich 1997).

In addition to this canonical scenario, another common scenario is to place the circular cylinder close to a plane boundary (e.g. ground or seabed), for which the flow is governed by not only Re, but also the plane boundary, whose effects may include

  (i) the near-wall effect, which is governed by the gap-to-diameter ratio G/D,
 (ii) the boundary layer effect, which is governed by the boundary layer thickness δ/D and shape factor (which are further governed by the streamwise distance between the leading edge of the plane boundary and the location of the cylinder for the streamwise evolution of the boundary layer),
(iii) boundary-layer-induced shear flow (rather than uniform approaching flow) incidence on the cylinder (for the case of $\delta > G$),
 (iv) boundary-layer-induced turbulence (rather than steady approaching flow) around the cylinder,
  (v) boundary-layer-induced mean streamwise velocity reduction at the location of the cylinder (for the case of $\delta > G$), etc.

The scenario of flow past a circular cylinder in proximity to a plane boundary has been studied extensively in the literature by both physical experiments (e.g. Bearman & Zdravkovich 1978; Grass *et al.* 1984; Zdravkovich 1985*a*; Taniguchi & Miyakoshi 1990; Lei, Cheng & Kavanagh 1999; Price *et al.* 2002; Wang & Tan 2008; Lin *et al.* 2009; He *et al.* 2017; Liu, Liu & Gao 2023) and numerical simulations (e.g. Lei *et al.* 2000; Ong *et al.* 2010; Thapa *et al.* 2014; Chen *et al.* 2022; Li *et al.* 2022). Because this scenario is governed by a very large parameter space (Re, G/D, δ/D, shape factor, shear rate, etc.), each of the previous studies generally focused on the effect of one or two parameters over certain regions of the parameter space. An extensive literature review of the previous studies suggested that, within this large parameter space, G/D was a key parameter that governed the flow characteristics and hydrodynamic forces. For example, for Re in the subcritical regime of $\sim 10^3$–10^5, the regular/alternate primary (Kármán) vortex shedding was generally suppressed at a critical G/D within 0.2–0.5 (e.g. Bearman & Zdravkovich 1978; Grass *et al.* 1984; Lei *et al.* 1999; Price *et al.* 2002; Wang & Tan 2008; Lin *et al.* 2009; He *et al.* 2017), and below which a single row of vortices may develop on the side of the cylinder away from the plane boundary (Bearman & Zdravkovich 1978; Price *et al.* 2002; Wang & Tan 2008; Lin *et al.* 2009; He *et al.* 2017). In addition, the mean drag and root-mean-square lift coefficients displayed relatively clear variation trends with the variation in G/D (Lei *et al.* 1999). Nevertheless, the flow and hydrodynamic characteristics were also affected by other parameters, e.g. δ/D (Grass *et al.* 1984; Taniguchi & Miyakoshi 1990; Lei *et al.* 1999), shape factor (Grass *et al.* 1984; Lin *et al.* 2009) and shear rate (Lei *et al.* 1999; Liu *et al.* 2023), whose effects may be less clear and more complicated, which made it difficult to confidently isolate the effect of the key parameter G/D and to attribute the observed flow features to certain effects/parameters. For example, different studies created different boundary layers and obtained different critical G/D values (generally within 0.2–0.5) for the suppression of alternate vortex shedding.

983 A18-2

To tackle this difficulty, the present study investigates the scenario of flow past a circular cylinder in proximity to a plane boundary that moves at a velocity equal to the free stream velocity. The use of a moving wall eliminates the streamwise evolution of the boundary layer (and the associated parameters including δ/D, shape factor, shear rate, etc.), which allows for a 'clean' examination of the near-wall effect. The variations in the flow and hydrodynamic characteristics and their physical mechanisms can thus be confidently attributed to the governing parameters *Re* and *G/D*.

The case of flow past a circular cylinder in proximity to a moving wall (or equally a body translating in still fluid parallel to a stationary wall) has also been studied extensively in the literature. An extensive literature review showed that most of the previous studies (mainly numerical) focused on relatively small *Re* of $\lesssim 300$ (over the laminar and three-dimensional (3-D) wake transition regimes), and reported rich flow and hydrodynamic characteristics which were highly dependent on both *Re* and *G/D*. Among which, Huang & Sung (2007), Yoon *et al.* (2010), Rao *et al.* (2011, 2013) and Jiang *et al.* (2017*a*) reported flow and hydrodynamic characteristics in the laminar regime through two-dimensional direct numerical simulations (DNS). Rao *et al.* (2013), Jiang *et al.* (2017*a*) and Wang *et al.* (2020) examined the onset of three-dimensionality through either linear stability analysis or 3-D DNS. In addition, Jiang *et al.* (2017*b*) examined the flow and hydrodynamic characteristics over the 3-D wake transition regimes up to $Re \sim 300$ and reported a 3-D wake regime map covering the (*Re*, *G/D*) parameter space. Beyond the 3-D wake transition regimes, physical experiments were conducted by Zdravkovich (1985*b*) at $Re = 3550$ and by Nishino, Roberts & Zhang (2007) at $Re = 4 \times 10^4$. Zdravkovich (1985*b*) observed alternate vortex shedding at $G/D = 0.6$ and a single row of vortices at $G/D = 0.1$, which was consistent with the general conclusions drawn from the scenario of a stationary wall. However, Nishino *et al.* (2007) reported a complete suppression of vortices from both sides of the cylinder for $G/D < 0.35$, which appeared at odds with Zdravkovich (1985*b*).

The previous studies have led to a good understanding of the flow and hydrodynamic characteristics over the laminar and 3-D wake transition regimes of $Re \lesssim 300$. However, to the best knowledge of the authors, the regime of wake transition to turbulence (which is closer to practical applications) has not been investigated in the literature, and a consensus on the vortex shedding pattern in the turbulent regime has not been reached. Motivated by these knowledge gaps, the present study will examine in detail the flow, hydrodynamic and turbulence characteristics for a circular cylinder in proximity to a moving wall over the parameter space of $Re = 300$–1000 and $G/D = 0.2$–3, where $Re = 300$ sits just beyond the 3-D wake transition regimes (Jiang *et al.* 2017*b*), while $Re = 1000$ represents a fully turbulent wake. In total, five different *Re* and 10 different *G/D* are considered, which resulted in a total of 50 3-D DNS cases in the (*Re*, *G/D*) parameter space.

2. Numerical model

2.1. *Numerical method*

Three-dimensional DNS were performed in the present study. The governing equations were the continuity and incompressible Navier–Stokes equations,

$$\frac{\partial u_i}{\partial x_i} = 0, \tag{2.1}$$

$$\frac{\partial u_i}{\partial t} + u_j \frac{\partial u_i}{\partial x_j} = -\frac{1}{\rho}\frac{\partial p}{\partial x_i} + \nu \frac{\partial^2 u_i}{\partial x_j \partial x_j}, \tag{2.2}$$

where $(x_1, x_2, x_3) = (x, y, z)$ are Cartesian coordinates, u_i is velocity component in the direction x_i, t is time, ρ is fluid density, p is pressure and ν is kinematic viscosity. Equations (2.1) and (2.2) were solved by the unsteady incompressible Navier–Stokes solver embedded in the open-source code Nektar++ (Cantwell *et al.* 2015), together with the use of a velocity correction scheme (Karniadakis, Israeli & Orszag 1991), a second-order implicit–explicit time-integration scheme and a continuous Galerkin projection. The global linear system was solved by using a parallel Cholesky factorisation based on the XX^T library, and the static condensation technique was applied repeatedly to reduce the system size and to improve the computational efficiency (Karniadakis & Sherwin 2005).

For the quasi-3-D cylinder investigated in the present study, the flow in the plane perpendicular to the cylinder axis (i.e. the x–y plane) was solved by a high-order spectral/*hp* element method (Karniadakis & Sherwin 2005), while that along the spanwise direction was expressed by a Fourier expansion (Karniadakis 1990), which took advantage of the spanwise homogeneity of the cylindrical body. This approach offers a greater efficiency than conventional finite element and similar approaches (Cantwell *et al.* 2015; Moxey *et al.* 2020). For example, Jiang & Cheng (2021) simulated a canonical case of flow past an isolated cylinder at $Re = 3900$ using both Nektar++ (based on the above-mentioned approach) and OpenFOAM (based on the conventional finite volume method), and found that for a similar level of numerical accuracy the computational cost for the former was only a few per cent of that for the latter. This evidence forms the rationale for the use of the Nektar++ approach for the present simulations.

To stabilise the solution, a spectral vanishing viscosity (SVV) technique (Kirby & Sherwin 2006), which increased the viscosity on the expansion modes with the highest frequencies, was employed to both the x–y plane and the spanwise direction. In addition, a spectral/*hp* dealiasing technique (Kirby & Sherwin 2006) was used in the x–y plane. Based on the Nektar++ User Guide, the default SVV cutoff ratio was 0.75, i.e. the lowest 75 % of the frequencies were not damped, while the SVV diffusion coefficient was 0.1. Based on a parameter dependence study of the SVV coefficients, Jiang & Cheng (2021) showed that the default SVV coefficients had negligible influence on the hydrodynamic forces on an isolated cylinder at $Re = 3900$. For a decreased Re of 1000, Jiang *et al.* (2022) showed that an increased SVV cutoff ratio of 0.9 and a SVV diffusion coefficient of 0.1 were sufficient to ensure numerical stability, and the turbulence characteristics in the cylinder wake were unaffected by the SVV diffusion (under the requisite that the mesh resolution was adequate). Therefore, for the present study with Re up to 1000, the SVV coefficients were the same as those used by Jiang *et al.* (2022).

2.2. *Computational domain and mesh*

As shown in figure 1(*a*), the present 3-D DNS adopted a rectangular computational domain in the x–y plane. The centre of the cylinder was located at the origin of the x–y plane. The computational domain size from the centre of the cylinder to the inlet, outlet and top boundaries was $60D$. The boundary conditions for the velocity included a uniform streamwise velocity U for the inlet and bottom boundaries, a Neumann condition (i.e. zero normal gradient) for the outlet boundary, a symmetry plane for the top boundary and a no-slip condition for the cylinder surface. The boundary conditions for the pressure included a reference of zero for the outlet boundary, and a high-order Neumann condition (Karniadakis *et al.* 1991) for all other boundaries. At the two planes perpendicular to the cylinder axis, periodic boundary conditions were imposed.

In the x–y plane, the perimeter of the cylinder was discretised with 48 macroelements, while the height of the first layer of elements next to the cylinder or moving wall
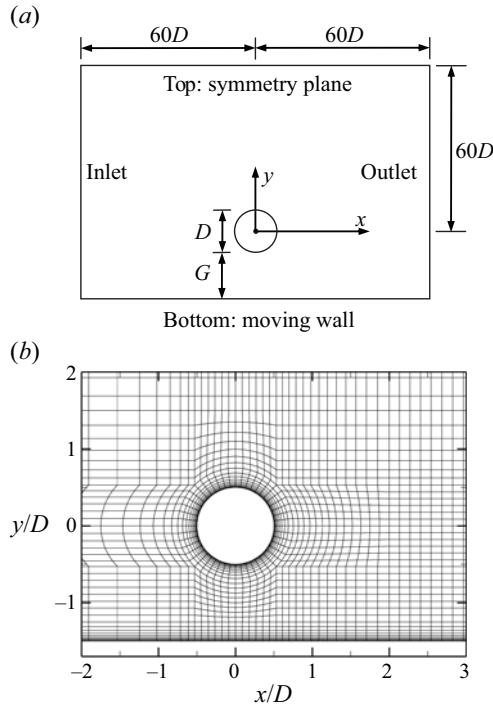
Figure 1. Computational domain and mesh in the x–y plane. (*a*) Schematic model of the computational domain (not to scale), and (*b*) close-up view of the macroelement mesh near the cylinder for the case of $G/D = 1$.

was $0.00587D$. The element expansion ratio was kept below 1.3. A relatively high mesh resolution was used in the wake region up to $x/D = 30$. Specifically, the streamwise size of the macroelements varied linearly from $0.13D$ at $x/D = 2$ to $0.40D$ at $x/D = 30$. The total number of macroelements in the x–y plane varied from 7775 for $G/D = 0.2$ to 15387 for $G/D = 3$. Figure 1(*b*) shows a close-up view of the macroelement mesh near the cylinder for an example of $G/D = 1$.

In addition to the h-type macroelement mesh, the p-type refinement allows for the subdivision of each macroelement using Lagrange polynomials on the Gauss–Lobatto–Legendre points for the quadrilateral expansion. In the present study, fourth-order Lagrange polynomials (denoted $N_p = 4$) were used for the cases of $Re = 400$–1000, while $N_p = 3$ was used for $Re = 300$. The N_p values were chosen based on a mesh dependence study reported in § 2.3.

Along the spanwise direction, different spanwise domain lengths (L_z/D) and spanwise resolutions ($\Delta z/D$) were used for different Re values. For $Re = 300$, 128 Fourier planes were used over $L_z/D = 12$ (with $\Delta z/D$ of 0.094), because Jiang *et al.* (2016) demonstrated the adequacy of $L_z/D = 12$ and $\Delta z/D = 0.1$ for the case of an isolated cylinder via domain size and mesh dependence studies. For $Re = 400$–1000, the present study used a smaller L_z/D of 6, because (i) numerically, Jiang & Cheng (2017) demonstrated the adequacy of $L_z/D = 6$ for the case of an isolated cylinder at both $Re = 400$ and 1000, and (ii) physically, beyond the wake transition regimes of Re up to $\sim$300 (Jiang *et al.* 2017*b*), the three-dimensionality of the wake was dominated by small-scale rib-like mode B structures (with spanwise wavelength of less than $1.0D$), such that $L_z/D = 6$ can accommodate at least

Case	N_p	Time range for statistics	St	$\overline{C_D}$	$\overline{C_L}$	C_L'
Reference case	4	700 time units ($\sim150T$)	0.216	1.147	0.0744	0.220
Variation case 1	3	700 time units ($\sim150T$)	0.217	1.159	0.0712	0.244
Variation case 2	4	350 time units ($\sim75T$)	0.216	1.152	0.0745	0.230

Table 1. Mesh dependence check for $(Re, G/D) = (1000, 1.0)$.

six spanwise periods of the mode B structures. Over the present L_z/D of 6, 128 Fourier planes were used to resolve the flow. This spanwise resolution was identical to that used by Jiang *et al.* (2022) for the DNS of an isolated cylinder at $Re = 1000$.

At the beginning of each simulation, the internal flow followed an impulsive start. The time step size was chosen based on a Courant–Friedrichs–Lewy limit of 0.6, which corresponded to non-dimensional time step sizes ($\Delta t^* = \Delta t U/D$) of ~0.003–0.005 for different cases. Each case was simulated for at least 600 non-dimensional time units (defined as $t^* = tU/D$). Among which, the statistics was performed over at least 375 non-dimensional time units, which corresponded to at least 80 vortex shedding periods (T). The sampling rate for the hydrodynamic quantities was $5\Delta t^*$, which was more than two orders of magnitude smaller than T. The sampling rate for the Reynolds stresses (and the turbulent kinetic energy (TKE)) was Δt^*. The extremely fine sampling rate was possible because the time-averaged Reynolds stresses could be easily calculated and updated during the simulation process (without outputting instantaneous flow fields for postprocessing). The sampling rate for the kinetic energy dissipation rate (determined via postprocessing) was $T/16$, which was deemed adequate by a sampling rate dependence check reported by Jiang *et al.* (2022).

2.3. *Mesh dependence study*

A 3-D mesh dependence study was performed for the case $(Re, G/D) = (1000, 1.0)$. Based on the reference case described in § 2.2, two variation cases were tested.

(i) Variation case 1: the N_p value decreased from 4 to 3.
(ii) Variation case 2: the time range for statistics changed from 700 non-dimensional time units for the reference case to 350 time units (by using only the first half of statistical data).

Table 1 summarises the numerical results obtained with the three cases, where the Strouhal number (St) and the drag and lift coefficients (C_D and C_L) are defined as

$$St = \frac{f_L D}{U}, \tag{2.3}$$

$$C_D = \frac{F_D}{\frac{1}{2}\rho U^2 D L_z}, \tag{2.4}$$

$$C_L = \frac{F_L}{\frac{1}{2}\rho U^2 D L_z}, \tag{2.5}$$

where F_D and F_L are the drag and lift forces on the cylinder, respectively, and f_L is the frequency of the fluctuating lift force, which is determined as the peak frequency derived from the fast Fourier transform of the time history of C_L. The time-averaged drag and lift
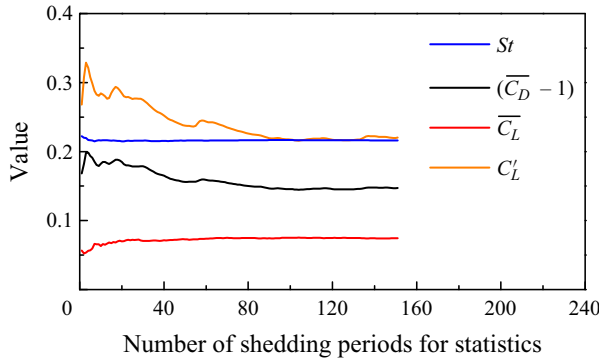
Figure 2. Dependence of hydrodynamic quantities on the number of shedding periods used for statistics. The time-averaged drag coefficient is deliberately subtracted by unity so as to be included in this figure.

coefficients are denoted $\overline{C_D}$ and $\overline{C_L}$, respectively. The root-mean-square lift coefficient is calculated as

$$C_L' = \sqrt{\frac{1}{N} \sum_{i=1}^{N} (C_{L,i} - \overline{C_L})^2}, \tag{2.6}$$

where N is the number of values in the time history.

As shown in table 1, the relatively good agreement between the reference case and variation case 1 suggested that $N_p = 3$ was marginally adequate for $Re = 1000$. Therefore, for the main body of the present study, $N_p = 4$ was adopted, while $N_p = 3$ was used for the smallest Re of 300 considered in this study. The close agreement between the reference case and variation case 2 suggested that 350 time units were adequate for the statistics. To further evaluate the adequacy of time range for statistics, figure 2 shows the dependence of hydrodynamic quantities on the number of shedding periods used for statistics. The hydrodynamic quantities converged when the statistical range included at least ∼80 shedding periods. Therefore, at least 80 shedding periods of statistical range were used for the present simulations.

To demonstrate the adequacy of the wake resolution in resolving the turbulence scales, Kolmogorov-scale normalised quantities were examined for the case of an isolated cylinder at the highest Re of 1000. The Kolmogorov time scale (τ_η) and length scale (η) are calculated as

$$\tau_\eta = \left(\frac{\nu}{\varepsilon}\right)^{1/2}, \tag{2.7}$$

$$\eta = \left(\frac{\nu^3}{\varepsilon}\right)^{1/4}, \tag{2.8}$$

where the kinetic energy dissipation rate ε is calculated as

$$\varepsilon = \nu \overline{\frac{\partial u_i}{\partial x_j}\left(\frac{\partial u_i}{\partial x_j} + \frac{\partial u_j}{\partial x_i}\right)}. \tag{2.9}$$

The Kolmogorov time and length scales along $y = 0$ (wake centreline) and $y/D = 0.577$ (centre of an element) are shown in figure 3(*a*,*b*). The Kolmogorov time scale ($\tau_\eta U/D > 0.1$) was much larger than the time step size ($\Delta t U/D = 0.003125$ for $Re = 1000$),
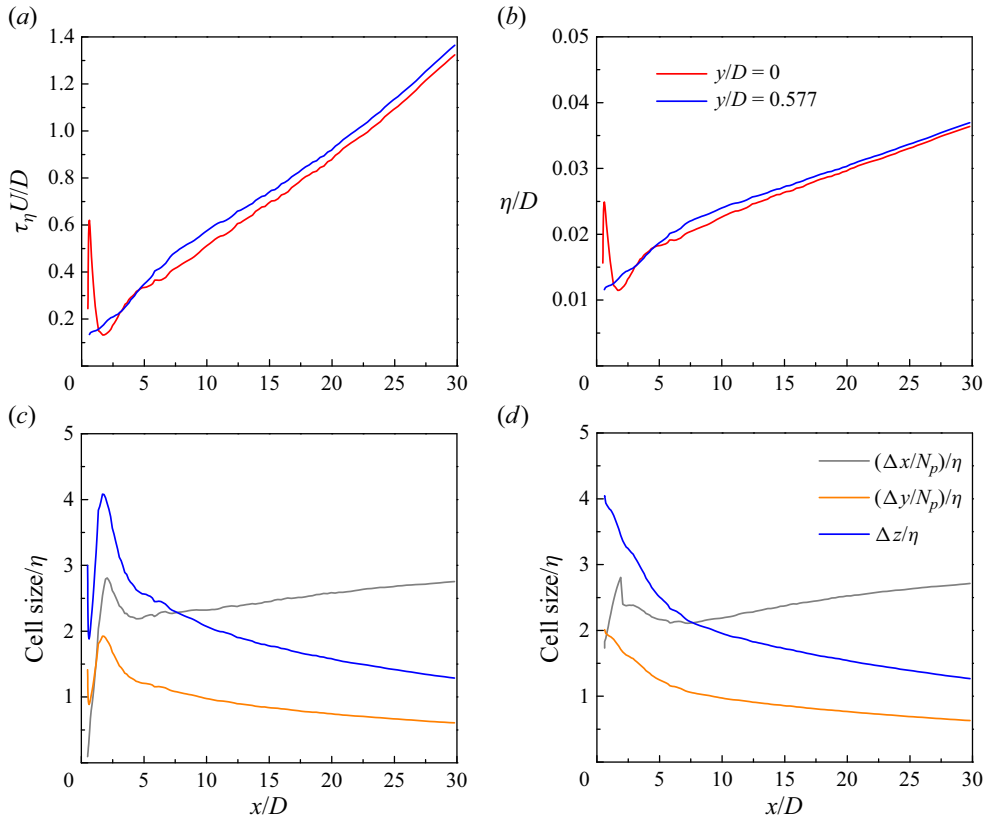
Figure 3. Streamwise variation of the Kolmogorov microscales and Kolmogorov-scale normalised quantities in the wake region of an isolated cylinder at $Re = 1000$: (a) Kolmogorov time scale τ_η; (b) Kolmogorov length scale η; (c) ratio between the cell size and η along $y = 0$; (d) ratio between the cell size and η along $y/D = 0.577$.

which ensured proper resolution of the time variation of turbulence. Figure 3(c,d) shows the ratio between the cell size (Δx, Δy and Δz) and η along $y/D = 0$ and 0.577, respectively. The cell size in the x–y plane was further divided by N_p to account for the p-type refinement of the macroelements. The Kolmogorov-scale normalised cell sizes were generally smaller than 4, i.e. the cell sizes were within the order of magnitude of the Kolmogorov length scale, which suggested that the mesh resolution was adequate in resolving the spatial variation of turbulence.

In addition, it is worth noting that the key properties of the reference mesh for $Re = 1000$ (including the topology of the macroelement mesh around the cylinder, $N_p = 4$, and 128 Fourier planes over $L_z/D = 6$) were very similar to those used by Jiang *et al.* (2022) for 3-D DNS of flow past an isolated cylinder at $Re = 1000$, where a detailed convergence check was conducted for quantities such as the hydrodynamic forces, wake recirculation length and turbulent dissipation rate in the wake.

3. Numerical results

3.1. *Instantaneous flow structures*

The instantaneous flow structures in the cylinder wake can be visualised by the streamwise vorticity (ω_x) and spanwise vorticity (ω_z) fields, where ω_x and ω_z are defined in a
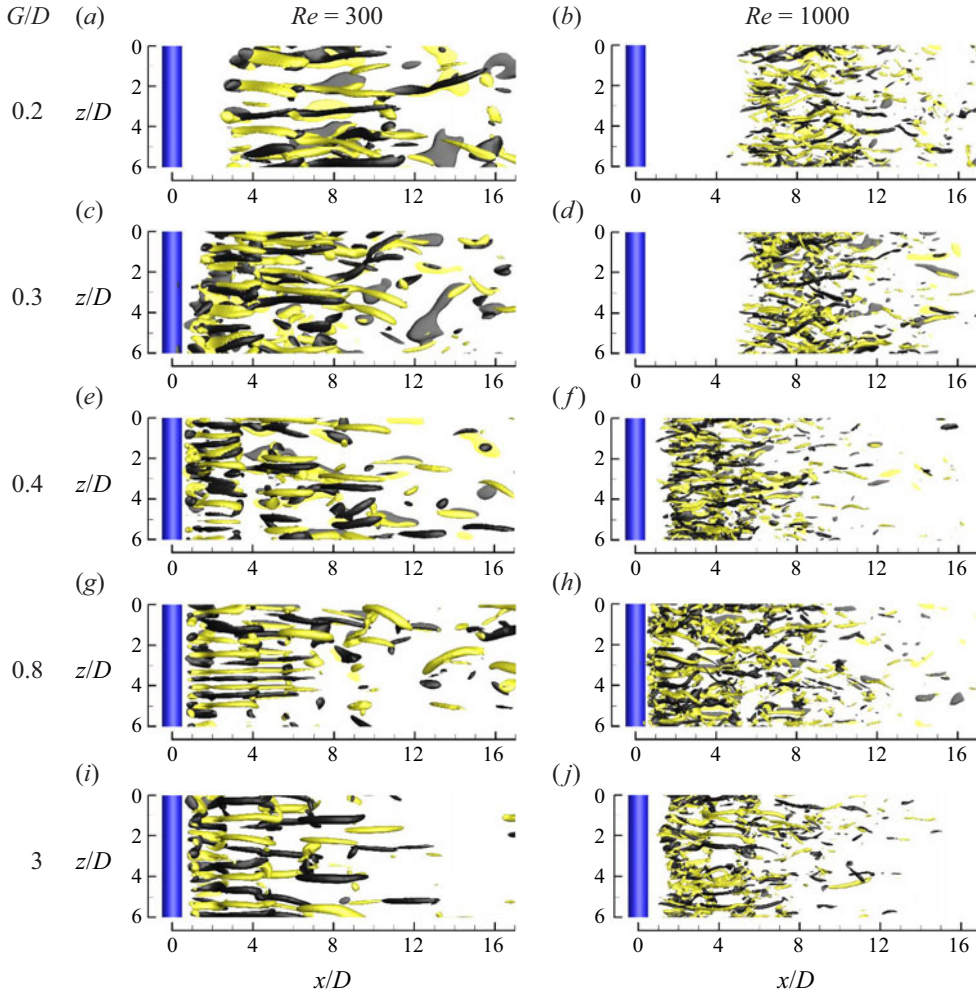
Figure 4. Instantaneous streamwise vorticity (ω_x) fields for the cases with various Re and G/D combinations. The isosurfaces are $\omega_x = \pm 1.5$ for $Re = 300$ and $\omega_x = \pm 5$ for $Re = 1000$. Dark grey and light yellow denote positive and negative vorticity values, respectively. The flow is from left to right past the cylinder on the left. Although the cases with $Re = 300$ are simulated with $L_z/D = 12$, the ω_x fields are shown with $z/D = 0$–6 so as to save space.

non-dimensional form as

$$\omega_x = \left(\frac{\partial u_z}{\partial y} - \frac{\partial u_y}{\partial z} \right) \frac{D}{U}, \tag{3.1}$$

$$\omega_z = \left(\frac{\partial u_y}{\partial x} - \frac{\partial u_x}{\partial y} \right) \frac{D}{U}. \tag{3.2}$$

Figure 4 presents an overview of the ω_x patterns for the cases with various Re and G/D combinations. Based on an examination of all the cases considered in this study (including those omitted in figure 4 due to space limit), it is found that beyond the complex wake transition regimes, the turbulent wakes of $Re \geq 300$ are always dominated by small-scale rib-like mode B structures. With the increase in Re from 300 to 1000, the mode B structures gradually become increasingly chaotic (figure 4), which signifies
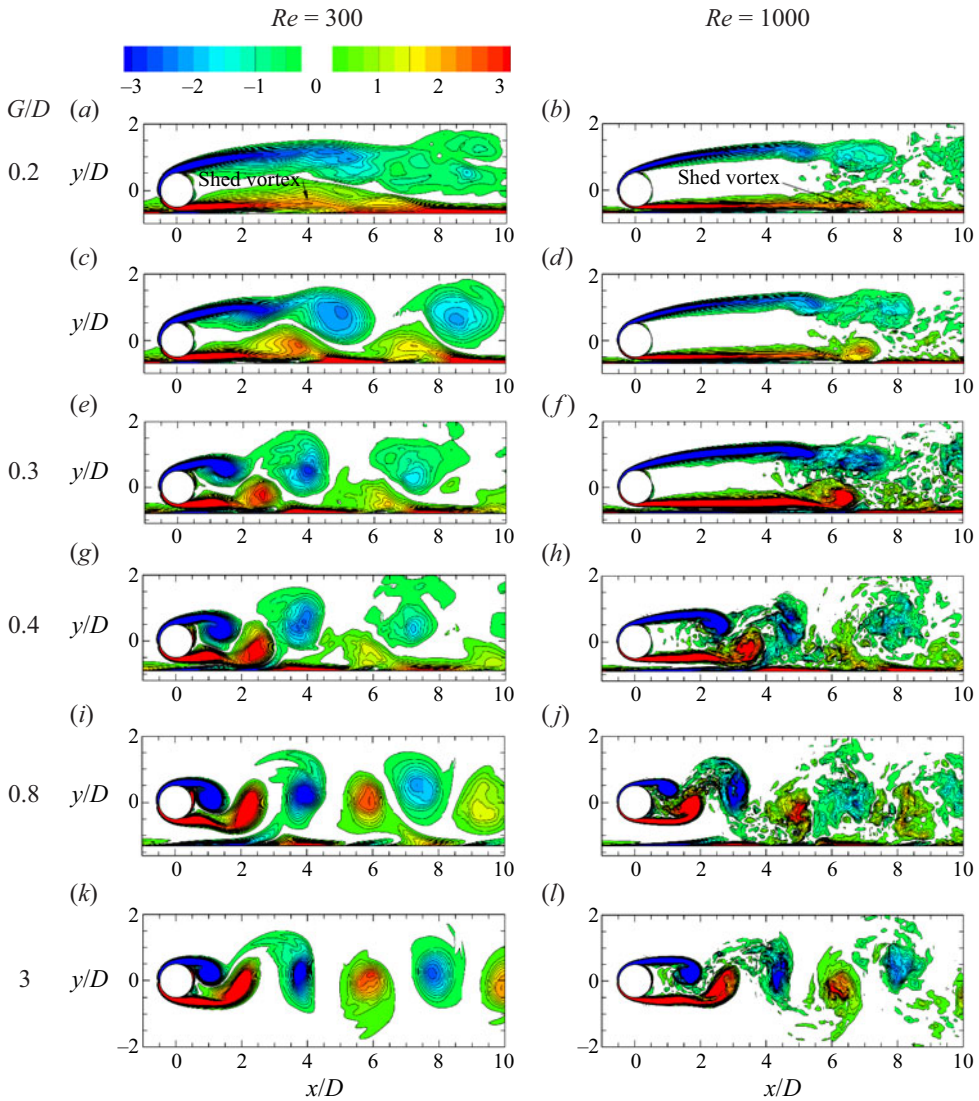
Figure 5. Instantaneous spanwise vorticity (ω_z) fields for the cases with various *Re* and *G/D* combinations. Each ω_z field is obtained from the corresponding span-averaged flow field and is shown at a phase when a lower (positive) vortex has just shed from the lower separating shear layer. The contours of ω_z are from -3 to 3, except for panels (*b*) and (*d*), where the contours are from -5 to 5.

increasingly turbulent wakes. On the other hand, the mode B structures are not noticeably influenced by *G/D*. The existence of solely mode B at *Re* ≥ 300 suggests that the flow and hydrodynamic characteristics (to be examined in §§ 3.2 and 3.3) may not experience sudden discontinuous changes in the present (*Re*, *G/D*) parameter space.

Figure 5 presents an overview of the vortex shedding (ω_z) patterns for the cases with various *Re* and *G/D* combinations. For each case, the ω_z field is shown at a phase when a lower (positive) vortex has just shed from the lower separating shear layer. Overall, alternate vortex shedding is observed for all the cases examined in this study (including those omitted in figure 5 due to space limits). With the increase in *Re* from 300 to

983 A18-10

1000, both the streamwise vortices (figure 4) and spanwise vortices (figure 5) become increasingly chaotic. With the decrease in G/D, the vortex shedding (ω_z) patterns are increasingly affected by the plane boundary. For $G/D \geq 0.3$ (figure 5e–l), alternate roll up and shedding of the vortices can be clearly observed in each and every vortex shedding period. For $G/D = 0.2$, alternate roll up and shedding of the vortices can be observed over the majority (approximately two thirds) of the vortex shedding periods (e.g. figure 5c,d), but within some vortex shedding periods the lower separating shear layer hardly rolls up, and under such circumstance a very weak lower (positive) vortex is shed directly from the lower separating shear layer (e.g. figure 5a,b). In between of the neighbouring lower vortices, the upper (negative) vortices shed from the cylinder induce shear layers on the plane boundary with positive sign of vorticity. The newly shed weak lower vortex is then quickly annihilated or merged into the shear layers developed on the plane boundary with the same sign of vorticity. Strictly speaking, for $G/D = 0.2$ alternate vortex shedding (either with or without rolling up of the lower separating shear layer) still occurs for each and every vortex shedding period. However, without detailed numerical flow visualisation to capture the short-lived weak lower vortices, the shedding pattern may easily be classified as intermittent shedding from the lower separating shear layer. In any sense, at $G/D = 0.2$ the plane boundary alters the vortex shedding pattern.

In contrast to the scenario of flow past a cylinder in proximity to a stationary wall, where the intermediate range of G/D may be divided into several flow regimes with different types of interactions between the wall boundary layer and the lower shear layer generated by the cylinder (Price *et al.* 2002; He *et al.* 2017), the present results of a moving wall suggest that, without (i) the upstream wall boundary layer generated by a stationary wall, and (ii) very large velocity gradients towards the stationary wall (with $u_x = 0$ on the wall), the vortex shedding pattern for $G/D \geq 0.3$ remains very similar. Although shear layers also develop on a moving wall (as a result of the variation in the streamwise velocity in accordance with the propagation of shed vortices along the wake), these shear layers are much weaker than those generated on a stationary wall and thus do not alter the overall vortex shedding pattern.

At relatively small G/D, specifically smaller than a critical G/D within 0.2–0.5, the stationary wall suppresses the lower row of vortices (Bearman & Zdravkovich 1978; Price *et al.* 2002; Wang & Tan 2008; Lin *et al.* 2009; He *et al.* 2017). However, the present results of a moving wall show that the lower row of vortices still exists at $G/D = 0.2$. This difference suggests that for the scenario of a stationary wall, the lower row of vortices is largely suppressed by the development of the upstream wall boundary layer (rather than the near-wall effect). This finding may explain why different studies for the scenario of a stationary wall (by using different upstream wall boundary layers) obtained different critical G/D values for the suppression of alternate vortex shedding (generally between 0.2 and 0.5).

3.2. *Time-averaged flow characteristics*

As shown in figure 5, the streamwise location for the roll up and shedding of the spanwise vortices (and consequently the streamwise location for the development of the streamwise vortices shown in figure 4) depends strongly on both *Re* and G/D. This feature can be visualised and quantified more clearly by the streamlines obtained from the time- and span-averaged flow (figure 6), where the wake stagnation point (sketched in figure 7) provides an approximation of the streamwise location for the vortex shedding. By defining the wake recirculation length L_r as the streamwise distance from the centre of the cylinder to the wake stagnation point (figure 7), figure 8(a) summarises the L_r values for the cases
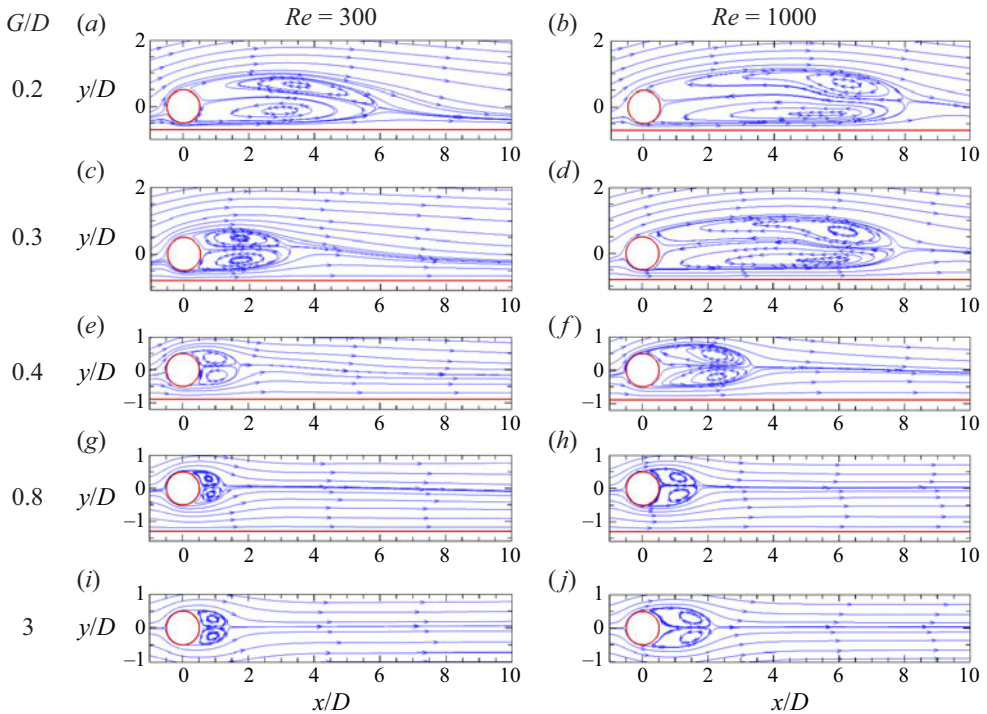
Figure 6. Streamlines of the time- and span-averaged flows for the cases with various Re and G/D combinations.
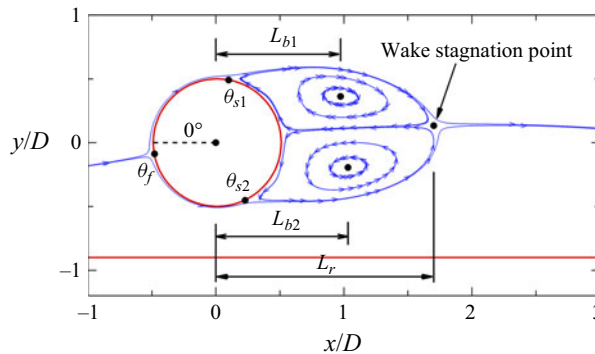

Figure 7. Definitions of the front stagnation point θ_f, upper separation angle θ_{s1}, lower separation angle θ_{s2}, upper bubble location L_{b1}, lower bubble location L_{b2} and wake recirculation length L_r, illustrated based on the case $(Re, G/D) = (300, 0.4)$. The blue curves represent streamlines of the time- and span-averaged flow, where two recirculation bubbles are observed behind the cylinder.

with various Re and G/D combinations. In general, for each Re the L_r value reaches to a local minimum at $G/D \sim 0.8$, while for each G/D the L_r value increases with increasing Re. The increase in L_r with increasing Re was also observed by Noca, Park & Gharib (1998) for an unbounded cylinder (i.e. $G/D \to \infty$). The consistent trend for the unbounded and near-wall scenarios suggests that the physical mechanism proposed for the unbounded scenario (Norberg 2003) may be applicable to the near-wall scenario. For an unbounded cylinder, Norberg (2003) suggested that 'the increase in secondary (essentially streamwise)
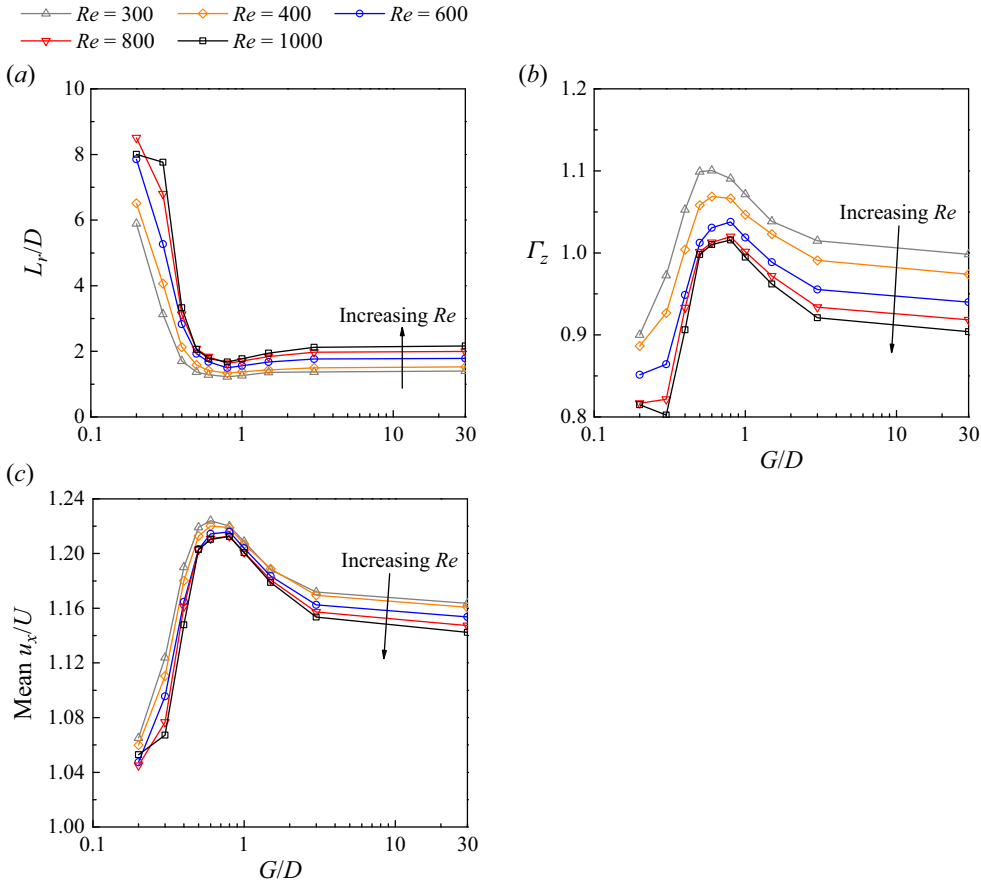
983 A18-12

Figure 8. Wake characteristics for flow past a circular cylinder in proximity to a moving wall, quantified by (*a*) the wake recirculation length L_r/D, (*b*) the mean spanwise circulation Γ_z past $x/D = 0.25$, and (*c*) the mean streamwise velocity sampled at $x = 0$ and within $1D$ both above and below the cylinder.

circulation occurs probably at the expense of the primary (essentially spanwise) circulation associated with the roll-up of the von Kármán vortices'. With the increase in *Re* from 300 to 1000, the increase in the streamwise circulation is expected, as the wake becomes increasingly turbulent (shown by the increasingly chaotic mode B structures in figure 4), while the reduction in the spanwise circulation is examined as follows. In the present study, we quantify the mean spanwise circulation (Γ_z) past $x/D = 0.25$ (i.e. feeding into the wake) per unit time. The mean circulation is obtained based on the time- and span-averaged flow field and is averaged between the upper and lower shear layers. The reason for the choice of $x/D = 0.25$ is that, at this point the shear layers have separated from the cylinder (such that there is no further accumulation of the circulation on the boundary layer), while the turbulence in the shear layer and wake (which may contribute undesirably to the sum of the circulation) have not yet developed. The Γ_z value is calculated as

$$\Gamma_z = \frac{1}{2} \left(\int_{upper\ shear\ layer} \frac{u_x}{U} |\omega_z| \, d\left(\frac{y}{D}\right) + \int_{lower\ shear\ layer} \frac{u_x}{U} |\omega_z| \, d\left(\frac{y}{D}\right) \right). \qquad (3.3)$$

Figure 8(*b*) shows the variation of Γ_z with *Re* and *G/D*, which confirms that the spanwise circulation reduces with increasing *Re* from 300 to 1000, and thus explains the increase in
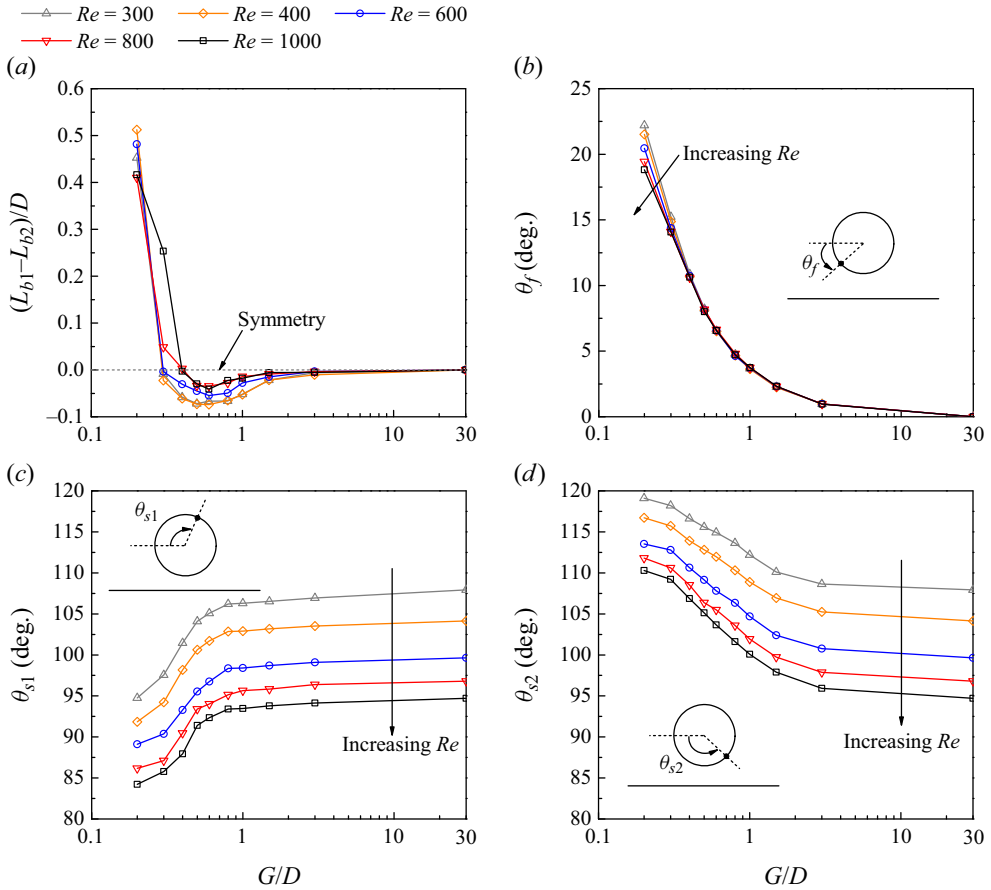
Figure 9. Flow asymmetry about the wake centreline, quantified by (*a*) the streamwise distance between the upper and lower bubble locations $(L_{b1}-L_{b2})/D$, (*b*) the front stagnation point θ_f, (*c*) the upper separation angle θ_{s1} and (*d*) the lower separation angle θ_{s2}.

L_r with increasing Re. Figure 8(*b*) also shows that for each Re, the spanwise circulation peaks at $G/D \sim 0.6$–0.8, which explains the local minimum in L_r at G/D around 0.8. The maximum spanwise circulation at $G/D \sim 0.6$–0.8 is physically linked to an increase in u_x around the cylinder at intermediate G/D due to blockage effects, and a decrease in u_x around the cylinder at small G/D due to flow deflection to the upper side of the cylinder. In figure 8(*c*), the u_x around the cylinder is quantified by the mean u_x sampled at $x = 0$ and within $1D$ both above and below the cylinder. Figure 8(*c*) confirms that the variation trend of this quantity resembles that of Γ_z. The quantitative differences between the variation trends shown in figure 8(*b*,*c*) is because the u_x around the cylinder also influences the ω_z around the cylinder, and they collectively shape the Γ_z value through (3.3).

The moving wall near the cylinder induces asymmetry of the flow about the wake centreline. The flow asymmetry is indicated by, for example, the non-zero streamwise distance between the upper and lower bubble locations $(L_{b1}-L_{b2})/D$ (figure 9*a*), the front stagnation point θ_f away from $0°$ (figure 9*b*) and different upper and lower separation angles (figure 9*c*,*d*). The definitions of these quantities are sketched in figure 7. Farther downstream, the flow asymmetry can be seen from the inclined streamlines shown in figure 6 (except for $G/D = 3$, where the flow asymmetry is negligible). Naturally, the level
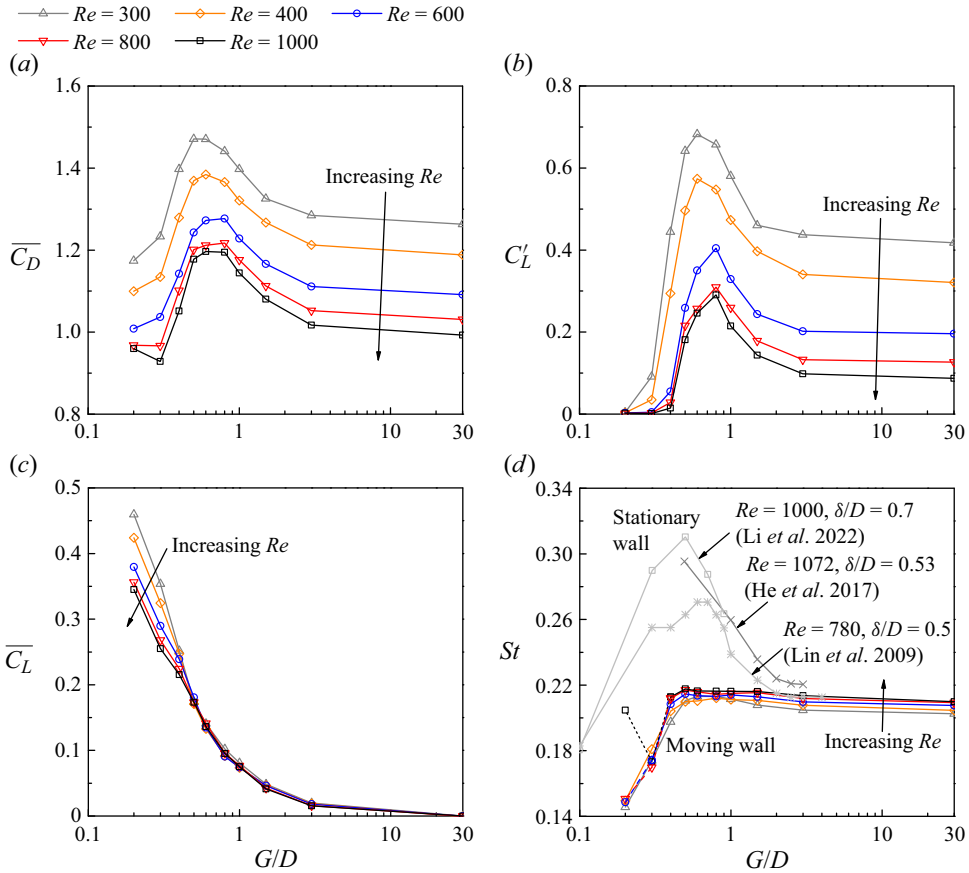
983 A18-14

Figure 10. Hydrodynamic characteristics for flow past a circular cylinder in proximity to a moving wall, quantified by (*a*) the time-averaged drag coefficient $\overline{C_D}$, (*b*) the root-mean-square lift coefficient C'_L, (*c*) the time-averaged lift coefficient $\overline{C_L}$ and (*d*) the Strouhal number St. For the majority of the cases, the St value is obtained via the C_L signal, whereas for the cases $(Re, G/D) = (600, 0.2)$, $(800, 0.2)$, $(1000, 0.2)$, $(800, 0.3)$ and $(1000, 0.3)$, the St value is obtained via the u_y signal, and the results are distinguished by the dashed lines.

of flow asymmetry increases with decreasing G/D. It is also seen in figure 9(*b–d*) that θ_f is insensitive to the variation in Re, whereas θ_{s1} and θ_{s2} vary with both Re and G/D. This difference stems from the condition of an unbounded cylinder, where θ_f remains at $0°$ for all Re values, whereas θ_{s1} and θ_{s2} vary with Re. The flow asymmetry can also be reflected by (and can explain) some of the hydrodynamic characteristics examined in § 3.3.

3.3. *Hydrodynamic characteristics*

Figure 10 summarises the hydrodynamic characteristics for the cases with various Re and G/D combinations. The close agreement between the results of $G/D = 3$ and 30 suggests that the effect of G/D becomes negligible at $G/D \gtrsim 3$. Below which, both G/D and Re may influence the hydrodynamic characteristics strongly.

Specifically, the variation trends of $\overline{C_D}$ (figure 10*a*) and C'_L (figure 10*b*) are generally consistent with that for Γ_z (figure 8*b*) and inversely correlated with that for L_r (figure 8*a*). The reduction in Γ_z and correspondingly the increase in L_r indicate downstream movement of the location for the vortex shedding, such that the alternate generation of the

low-pressure regions at the locations of the vortex cores exerts less contribution to the mean suction and fluctuating lift back on the cylinder. However, while L_r increases significantly at $G/D \lesssim 0.4$ (figure 8a), its effect on the reduction in $\overline{C_D}$ and C'_L seems less significant (figure 10a,b). This is because (i) the influence of the low pressure regions on the hydrodynamic forces is nonlinear (e.g. for $L_r/D \gtrsim 3$–4 the C'_L value approaches zero already), and (ii) unlike the C'_L value which is solely induced by the alternate generation of the low pressure regions in the near wake, the $\overline{C_D}$ value is also significantly contributed by the positive pressure force on the front side of the cylinder (such that for $L_r/D \gtrsim 3$–4, $\overline{C_D}$ does not approach zero).

Figure 10(c) shows the variation trend of $\overline{C_L}$, which resembles the variation trend of θ_f (figure 9b). With the downward movement of the front stagnation point, a net lift is expected.

Figure 10(d) shows the variation of St with Re and G/D. The St value stays at a similar level (within 0.20–0.22) for $G/D \geq 0.4$, but drops drastically with decreasing G/D below 0.4. An exception is observed for the case $(Re, G/D) = (1000, 0.2)$, where St remains at around 0.20 (to be closely examined later on). Figure 10(d) also shows the variation of St with G/D for the scenario of a stationary wall obtained experimentally by Lin *et al.* (2009), He *et al.* (2017) and Li *et al.* (2022). Their results indicate that St increases significantly as G/D decreases from approximately 2 to 0.5, but decreases with further decrease in G/D. A comparison between the stationary and moving wall results suggests that the increase in St over $G/D \sim 2$–0.5 for a stationary wall is attributed to the development of the upstream wall boundary layer, whereas the drastic reduction in St at $G/D \lesssim 0.4$ is due to the near-wall effect.

3.4. *Frequency spectra of lift and velocity signals*

The cases with $Re = 1000$ and different G/D values are used to further illustrate the characteristics of the vortex shedding frequency. Figure 11 shows the frequency spectra of the lift signal (C_L) sampled at the location of the cylinder (i.e. at $x \sim 0$), while figure 12 shows the frequency spectra of the transverse velocity signal (u_y) sampled at a location closer to the streamwise location of vortex shedding. This location is chosen at $x/D = L_r/D - 1$ and $y/D = 0.5$, and eight equally spaced spanwise locations are used to average the frequency spectrum. Figures 11(a) and 12(a) show the frequency spectra of C_L and u_y in linear scales, which reveal clearly the broad-bandedness and strength of the dominant frequencies. Figures 11(b) and 12(b) show the power spectra of C_L and u_y in logarithmic scales, where E_L and E_{uy} are calculated as

$$\int_0^\infty E_L \, \mathrm{d}\left(\frac{f}{f_L}\right) = C'^2_L, \tag{3.4}$$

$$\int_0^\infty E_{uy} \, \mathrm{d}\left(\frac{f}{f_{uy}}\right) = \frac{\overline{u'_y u'_y}}{U^2}. \tag{3.5}$$

The logarithmic scales may help reveal very weak frequencies which are difficult to be identified in linear scales.

For the present cases with various Re and G/D combinations, a common finding is that, for the cases with vortex shedding occurring relatively far from the cylinder (specifically with $L_r/D > 6.7$, see figure 8a), the St value can hardly be identified from the frequency spectra of C_L. For example, figure 11(a) shows the frequency spectra of C_L for the cases with $Re = 1000$ and various G/D, where the frequency peak becomes absent for $G/D \leq 0.3$
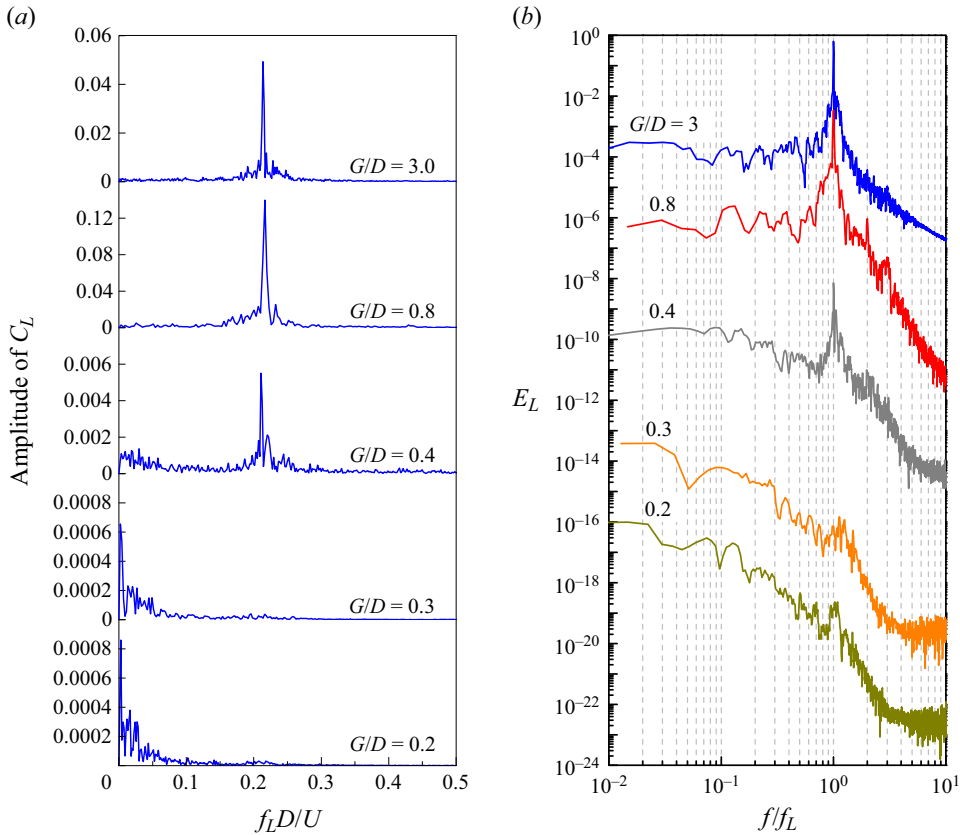
Figure 11. Frequency spectra of C_L for the cases with $Re = 1000$ and various G/D values: (*a*) frequency spectra of C_L in linear scales; (*b*) power spectra of C_L in logarithmic scales, where each spectrum (other than the top one) is shifted downward by three orders of magnitude.

(such that the noise level at $f_L \sim 0$, which is always of the order of magnitude of 10^{-3} for different G/D, becomes dominant).

With the aid of the logarithmic scales in figure 11(*b*), very weak vortex shedding frequency peaks may be observed for $G/D = 0.3$ and 0.2. Nevertheless, it is difficult to identify a definite St value, because there exists a broad-band region of frequencies without a dominant frequency peak (and the dominant frequency f_L required for plotting figure 11*b* is actually borrowed from f_{uy} identified in figure 12*a*), and the broad-band frequencies are only marginally above the noise level.

To obtain the dominant St values for $G/D = 0.3$ and 0.2, we instead use the u_y signals sampled at a location closer to the streamwise location of vortex shedding (i.e. $x/D = L_r/D - 1$ and $y/D = 0.5$). The St values obtained from the u_y signals are shown in figure 10(*d*) with dashed lines, and examples of frequency spectra of u_y for the cases with $Re = 1000$ are shown in figure 12. The case $G/D = 0.4$ confirms that the frequency spectra of C_L and u_y yield identical St, and flow visualisation of this case confirms that the time period for each vortex shedding cycle is indeed approximately $1/St$. For $G/D = 0.3$ and 0.2, the St values can hardly be determined from the C_L signal (figure 11), but can be revealed by a u_y signal sampled close to the location of vortex shedding (figure 12). The existence of a frequency peak in the u_y spectrum is consistent with the observation
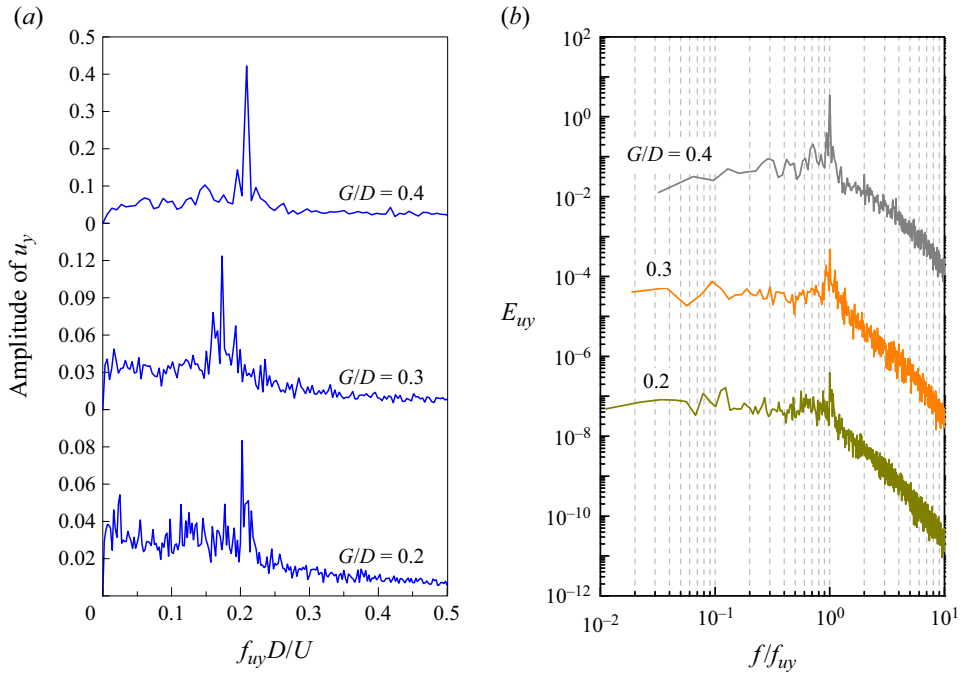
983 A18-17

Figure 12. Frequency spectra of u_y sampled at a location close to the streamwise location of vortex shedding (i.e. $x/D = L_r/D - 1$ and $y/D = 0.5$) for the cases with $Re = 1000$ and various G/D values: (*a*) frequency spectra of u_y in linear scales; (*b*) power spectra of u_y in logarithmic scales, where each spectrum (other than the top one) is shifted downward by three orders of magnitude.

of clear vortex shedding from flow visualisation (figure 5). Based on flow visualisation, it is also found that the time periods for different vortex shedding cycles may vary noticeably. The noticeable variation in the vortex shedding period is attributed to the time variation in strength of the positive vortices shed from the lower side of the cylinder (reflected by different degrees of rolling up before shedding) due to the near-wall effect. Consequently, the u_y spectra for $G/D = 0.3$ and 0.2 (figure 12*a*) are relatively broad-band. For $G/D = 0.2$, the frequency peak is only slightly larger than the amplitudes of a range of other frequencies, which partly explains why the St value for this case deviates from the general trend (figure 10*d*). For this case, the St value simply corresponds to a vortex shedding frequency that is slightly more dominant than others, but a range of other frequencies are also observed in figure 12(*a*).

Another key finding is that, a negligible frequency peak with no dominant St value in the C_L spectrum does not necessarily indicate absence of, or negligible, vortex shedding phenomenon. The use of a readily available C_L spectrum as the criterion for the determination of the critical G/D for the suppression of vortex shedding (as was used by several previous studies for the case of a stationary wall) may lead to inaccurate conclusion.

3.5. *Turbulent kinetic energy*

This section examines the influence of Re and G/D on the mean TKE in the wake region. At each spatial location, the TKE is calculated as $(\overline{u'_x u'_x} + \overline{u'_y u'_y} + \overline{u'_z u'_z})/(2U^2)$, where
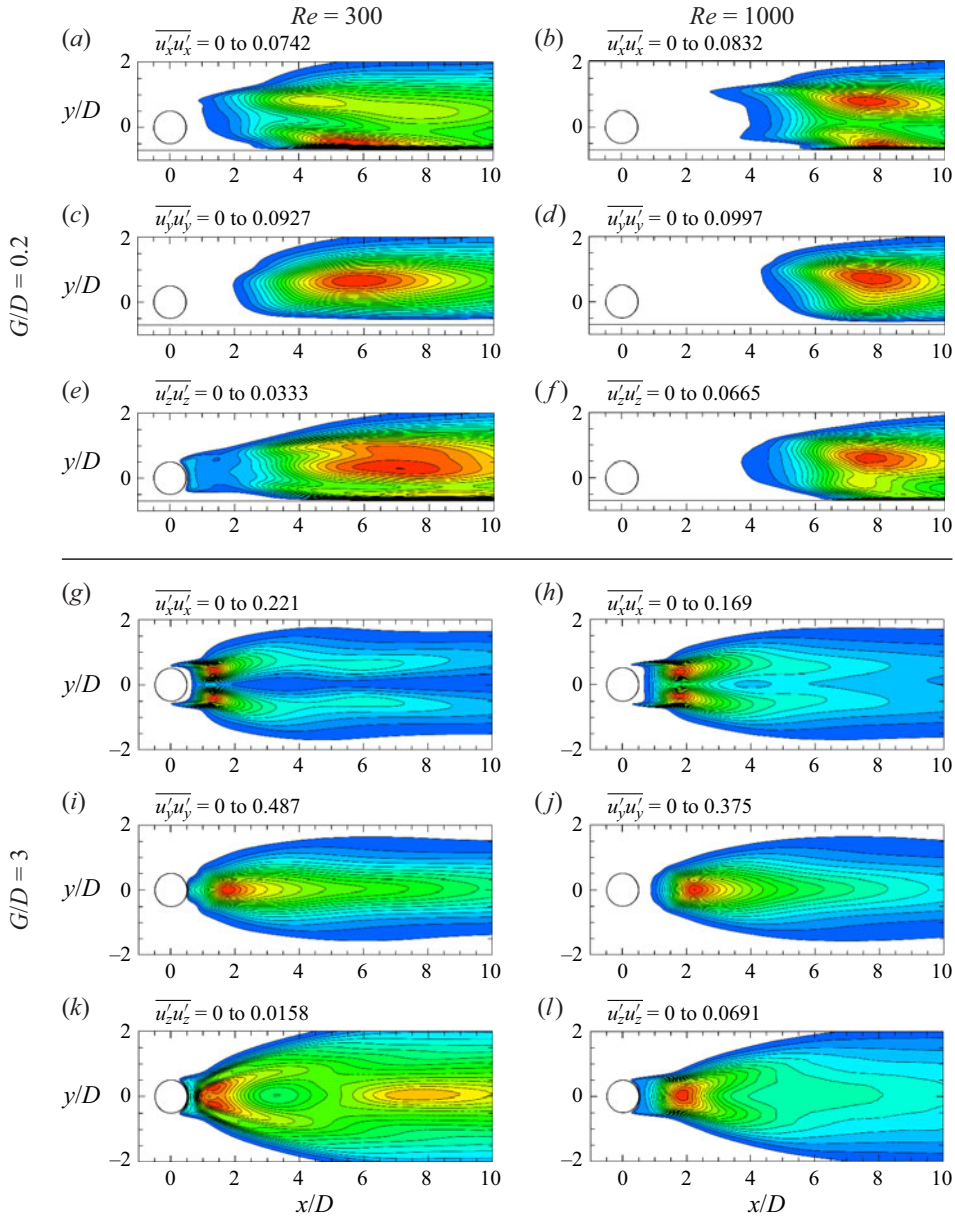
983 A18-18

Figure 13. Velocity fluctuation fields for the cases with various *Re* and *G/D* combinations. In each panel, the contours are from 0 to the maximum value with 20 equal intervals. The velocity components are normalised by *U* already.

$u_i' = u_i - \overline{u_i}$. Figure 13 illustrates the velocity variance fields for the cases with various *Re* and *G/D* combinations. The velocity variance patterns are significantly affected by *G/D* and relatively less affected by *Re*. For *G/D* = 3, the velocity variance patterns are largely symmetric about the wake centreline, whereas for *G/D* = 0.2, the patterns are significantly altered. Since different cases may display very different velocity variance patterns, it is less meaningful to simply compare the peak value or any specific spatial location. In the present study, the TKE (and its three components) of different cases are compared after
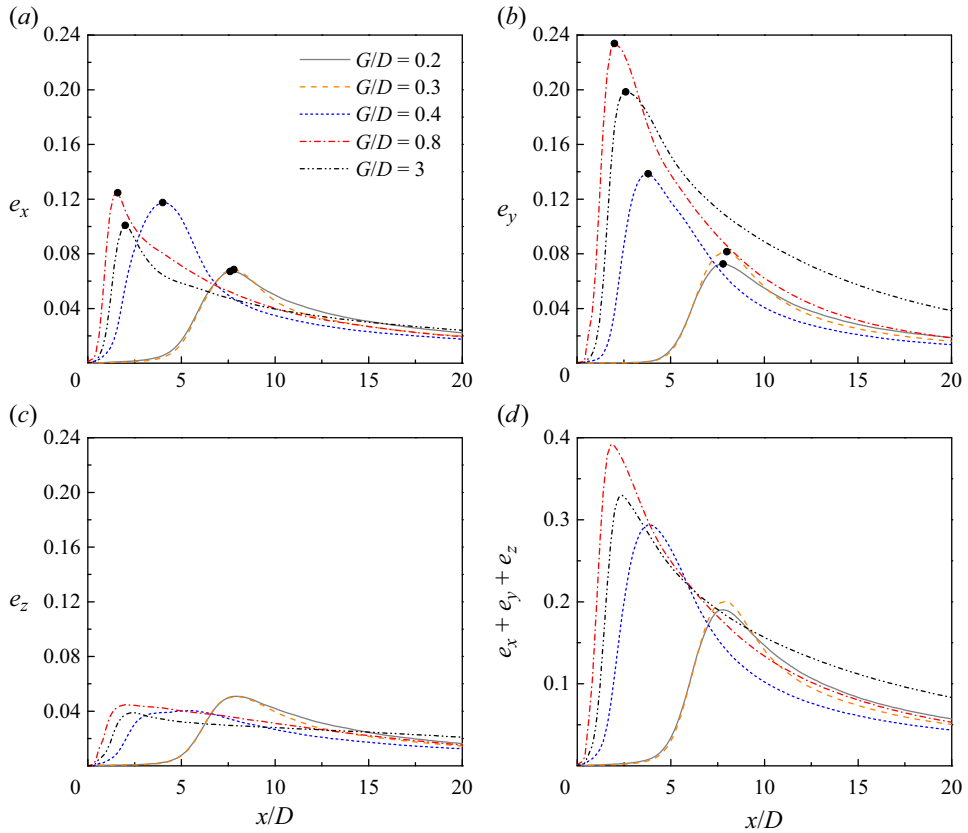
Figure 14. Integrated kinetic energy components for the cases with $Re = 1000$ and various G/D values: (*a*) the e_x component; (*b*) the e_y component; (*c*) the e_z component; (*d*) the sum of three components.

integrating the result along the *y*-direction, i.e.

$$e_x = \frac{1}{2} \int \frac{\overline{u'_x u'_x}}{U^2} \, \mathrm{d}\left(\frac{y}{D}\right), \tag{3.6}$$

$$e_y = \frac{1}{2} \int \frac{\overline{u'_y u'_y}}{U^2} \, \mathrm{d}\left(\frac{y}{D}\right), \tag{3.7}$$

$$e_z = \frac{1}{2} \int \frac{\overline{u'_z u'_z}}{U^2} \, \mathrm{d}\left(\frac{y}{D}\right). \tag{3.8}$$

Figure 14 shows the integrated kinetic energy components for the cases with $Re = 1000$ and various G/D values. For each case, the relative strengths of the three energy components generally follow $e_y > e_x > e_z$. The anisotropy of the kinetic energy in the wake is largely due to the contribution of the primary vortices to e_y and e_x. For example, Jiang *et al.* (2022) investigated the case of an unbounded cylinder (i.e. $G/D \to \infty$) at $Re = 1000$ and examined the anisotropy of the kinetic energy at $x/D = 10$ and 20 and found that, by removing the contribution of the primary vortices, the kinetic energy became much more isotropic. For the present cases with different G/D, the maximum e_z value stays consistently at ~ 0.04–0.05 (since e_z is not directly contributed by the primary vortices), whereas the maximum e_x and e_y values (highlighted by dots in figure 14*a,b*) vary with
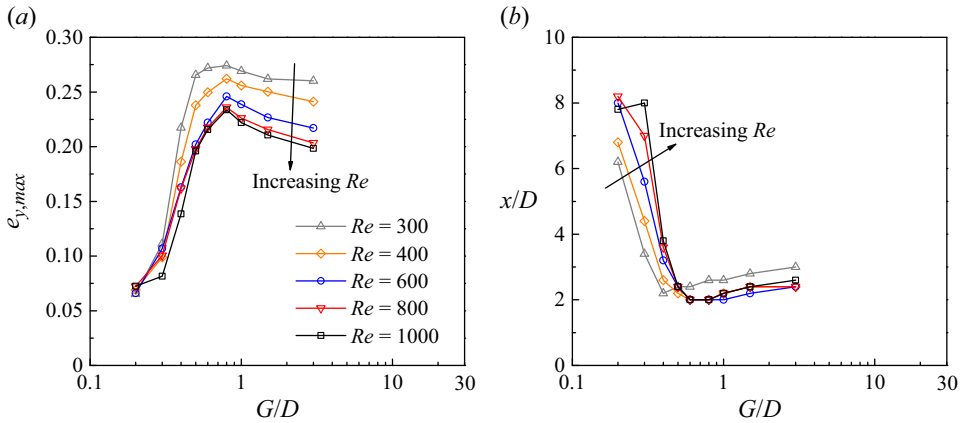
Figure 15. Characteristics of the maximum e_y for the cases with various Re and G/D combinations: (*a*) the magnitude, and (*b*) the streamwise location (with a resolution of $\Delta x/D = 0.2$).
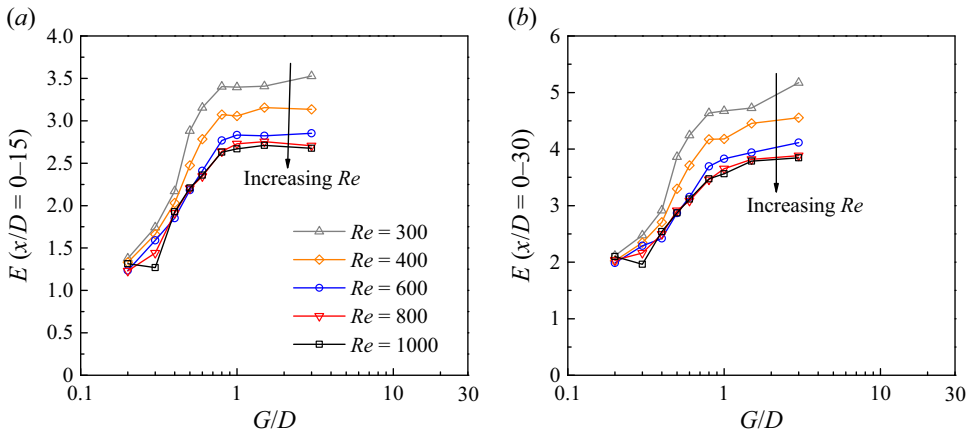

Figure 16. Variation of the total TKE in the wake region with Re and G/D: (*a*) over the wake region of $x/D = 0$–15, and (*b*) over the wake region of $x/D = 0$–30.

G/D, which suggests that for different G/D the contribution from the primary vortices may be different.

For the cases with various Re and G/D combinations, the magnitude and streamwise location for the maximum e_y values (denoted $e_{y,max}$) are plotted in figure 15. Although the kinetic energy in the wake is not solely contributed by this maximum value, it serves as a crude indication of the variation of the kinetic energy with the characteristics of the primary vortices. Specifically, the variation of $e_{y,max}$ (figure 15*a*) resembles that of Γ_z (figure 8*b*), while the variation of the streamwise location of $e_{y,max}$ (figure 15*b*) resembles that of L_r (figure 8*a*). These resemblances suggest that the strength and streamwise location of the shed primary vortices dictate the point of $e_{y,max}$ and thus influence strongly the kinetic energy in the wake.

Figure 16 shows the variation of the total TKE (E) in the wake region (per unit span length) with Re and G/D, where E is calculated as

$$E = \int (e_x + e_y + e_z)\, d\left(\frac{x}{D}\right). \tag{3.9}$$

Two different wake regions are considered, i.e. $x/D = 0$–15 (figure 16a) and $x/D = 0$–30 (figure 16b). Their similarity suggests that the variation trends are not significantly affected by the choice of the streamwise range. A major feature shown in figure 16 is that E reduces drastically as G/D reduces below 0.8. As discussed with the aid of $e_{y,max}$, the reduction of E is due to both (i) reduction in the strength of the shed vortices and (ii) downstream movement of the location of vortex shedding. In addition, with the downstream movement of the primary vortices, the streamwise vortices are also generated farther downstream (cf. figures 4 and 5), which leads to a delayed growth of e_z (figure 14c). The above-mentioned three factors contribute collectively to the significant reduction of E shown in figure 16.

4. Conclusions

This study examines the scenario of flow past a circular cylinder in proximity to a moving wall (or equally a body translating in still fluid parallel to a stationary wall) over the parameter space of $Re = 300$–1000 and $G/D = 0.2$–3. Visualisation of the streamwise vortices shows that the turbulent wakes of $Re \geq 300$ (beyond the wake transition regimes) are always dominated by small-scale rib-like mode B structures which gradually become increasingly chaotic with increasing Re. Visualisation of the spanwise vortices shows that alternate vortex shedding persists for all cases. The only distinctive feature is that, for $G/D = 0.2$ the shedding of the lower (positive) vortices may be relatively weak – for approximately one third of the vortex shedding periods the lower vortices are shed without rolling up of the separating shear layer.

Over the (Re, G/D) parameter space, the variations in the flow, hydrodynamic and turbulence characteristics and their underlying physical mechanisms are examined in detail. The major findings are summarised below.

(i) Flow characteristics. The streamwise location for the vortex shedding (quantified by L_r) depends strongly on both Re and G/D. In general, for each Re the L_r value reaches to a local minimum at $G/D \sim 0.8$, while for each G/D the L_r value increases with increasing Re. The variation of L_r with Re and G/D can be explained by the spanwise circulation Γ_z fed into the wake, where the variation trend of L_r is inversely correlated with that of Γ_z. The local maximum of Γ_z at $G/D \sim 0.6$–0.8 is physically linked to an increase in the streamwise velocity around the cylinder at intermediate G/D due to blockage effect, while the reduction in Γ_z with increasing Re is because the streamwise circulation draws increasing energy from the spanwise circulation.

(i) Hydrodynamic characteristics. The variation trends of the hydrodynamic coefficients $\overline{C_D}$ and C_L' are generally consistent with that of Γ_z and inversely correlated with that of L_r. Physically, when the location of vortex shedding moves downstream, the alternate generation of the low-pressure regions at the locations of the vortex cores exerts less contribution to the mean suction and fluctuating lift back on the cylinder. The variation trend of $\overline{C_L}$ is consistent with that of the front stagnation point θ_f. Physically, with the downward movement of the front stagnation point, a net lift is expected.

(iii) Turbulence characteristics. The total kinetic energy in the wake region reduces drastically as G/D reduces below 0.8. The reduction of E is contributed collectively by (i) reduction in the strength of the shed vortices, (ii) downstream movement of the location of vortex shedding and (iii) downstream movement of the location of the streamwise vortices associated with the delayed generation of primary vortices.

The present results on a moving wall also help to explain several flow and hydrodynamic characteristics reported in the literature for a stationary wall. For example, the existence of

alternate vortex shedding for a moving wall at $G/D = 0.2$ suggests that the suppression of the lower row of vortices for a stationary wall at $G/D = 0.2$–0.5 is due to the development of the upstream wall boundary layer (rather than the near-wall effect), and different wall boundary layers may result in different critical G/D values between 0.2 and 0.5. A comparison between the stationary and moving wall results also suggests that, the increase in *St* over $G/D \sim 2$–0.5 for a stationary wall is attributed to the development of the upstream wall boundary layer, whereas the drastic reduction in *St* at $G/D \lesssim 0.4$ is attributed to the near-wall effect.

Declaration of interests. The authors report no conflict of interest.

Author ORCIDs.

Hongyi Jiang https://orcid.org/0000-0002-0137-6355;

Xiaoying Ju https://orcid.org/0000-0002-0976-4918.

REFERENCES

BEARMAN, P.W. & ZDRAVKOVICH, M.M. 1978 Flow around a circular cylinder near a plane boundary. *J. Fluid Mech.* **89**, 33–47.

CANTWELL, C.D., *et al.* 2015 Nektar++: an open-source spectral/hp element framework. *Comput. Phys. Commun.* **192**, 205–219.

CHEN, W., JI, C., ALAM, M.M., XU, D. & ZHANG, Z. 2022 Three-dimensional flow past a circular cylinder in proximity to a stationary wall. *Ocean Engng* **247**, 110783.

GRASS, A.J., RAVEN, P.W.J., STUART, R.J. & BRAY, J.A. 1984 The influence of boundary layer velocity gradients and bed proximity on vortex shedding from free spanning pipelines. *J. Energy Resour. Technol.* **106**, 70–78.

HE, G.S., WANG, J.J., PAN, C., FENG, L.H., GAO, Q. & RINOSHIKA, A. 2017 Vortex dynamics for flow over a circular cylinder in proximity to a wall. *J. Fluid Mech.* **812**, 698–720.

HUANG, W.X. & SUNG, H.J. 2007 Vortex shedding from a circular cylinder near a moving wall. *J. Fluids Struct.* **23**, 1064–1076.

JIANG, H. & CHENG, L. 2017 Strouhal–Reynolds number relationship for flow past a circular cylinder. *J. Fluid Mech.* **832**, 170–188.

JIANG, H. & CHENG, L. 2021 Large-eddy simulation of flow past a circular cylinder for Reynolds numbers 400 to 3900. *Phys. Fluids* **33**, 034119.

JIANG, H., CHENG, L., DRAPER, S. & AN, H. 2017*a* Two- and three-dimensional instabilities in the wake of a circular cylinder near a moving wall. *J. Fluid Mech.* **812**, 435–462.

JIANG, H., CHENG, L., DRAPER, S. & AN, H. 2017*b* Three-dimensional wake transition for a circular cylinder near a moving wall. *J. Fluid Mech.* **818**, 260–287.

JIANG, H., CHENG, L., DRAPER, S., AN, H. & TONG, F. 2016 Three-dimensional direct numerical simulation of wake transitions of a circular cylinder. *J. Fluid Mech.* **801**, 353–391.

JIANG, H., HU, X., CHENG, L. & ZHOU, T. 2022 Direct numerical simulation of the turbulent kinetic energy and energy dissipation rate in a cylinder wake. *J. Fluid Mech.* **946**, A11.

KARNIADAKIS, G.E. 1990 Spectral element-Fourier methods for incompressible turbulent flows. *Comput. Meth. Appl. Mech. Engng* **80**, 367–380.

KARNIADAKIS, G.E., ISRAELI, M. & ORSZAG, S.A. 1991 High-order splitting methods for the incompressible Navier–Stokes equations. *J. Comput. Phys.* **97**, 414–443.

KARNIADAKIS, G.E. & SHERWIN, S.J. 2005 *Spectral/hp Element Methods for CFD*. Oxford University Press.

KIRBY, R.M. & SHERWIN, S.J. 2006 Stabilisation of spectral/hp element methods through spectral vanishing viscosity: application to fluid mechanics modelling. *Comput. Meth. Appl. Mech. Engng* **195**, 3128–3144.

LEI, C., CHENG, L., ARMFIELD, S.W. & KAVANAGH, K. 2000 Vortex shedding suppression for flow over a circular cylinder near a plane boundary. *Ocean Engng* **27**, 1109–1127.

LEI, C., CHENG, L. & KAVANAGH, K. 1999 Re-examination of the effect of a plane boundary on force and vortex shedding of a circular cylinder. *J. Wind Engng Ind. Aerodyn.* **80**, 263–286.

LI, J., WANG, B., QIU, X., WU, J., ZHOU, Q., FU, S. & LIU, Y. 2022 Three-dimensional vortex dynamics and transitional flow induced by a circular cylinder placed near a plane wall with small gap ratios. *J. Fluid Mech.* **953**, A2.

LIN, W.J., LIN, C., HSIEH, S.C. & DEY, S. 2009 Flow characteristics around a circular cylinder placed horizontally above a plane boundary. *J. Engng Mech.* **135**, 697–716.

LIU, Y., LIU, J. & GAO, F. 2023 Strouhal number for boundary shear flow past a circular cylinder in the subcritical flow regime. *Ocean Engng* **269**, 113574.

MOXEY, D., *et al.* 2020 Nektar++: enhancing the capability and application of high-fidelity spectral/hp element methods. *Comput. Phys. Commun.* **249**, 107110.

NISHINO, T., ROBERTS, G.T. & ZHANG, X. 2007 Vortex shedding from a circular cylinder near a moving ground. *Phys. Fluids* **19**, 025103.

NOCA, F., PARK, H. & GHARIB, M. 1998 Vortex formation length of a circular cylinder (300 < *Re* < 4000) using DPIV. In *Proceedings on Bluff Body Wakes and Vortex-Induced Vibration*. ASME Fluids Engineering Division.

NORBERG, C. 2003 Fluctuating lift on a circular cylinder: review and new measurements. *J. Fluids Struct.* **17**, 57–96.

ONG, M.C., UTNES, T., HOLMEDAL, L.E., MYRHAUG, D. & PETTERSEN, B. 2010 Numerical simulation of flow around a circular cylinder close to a flat seabed at high Reynolds numbers using a *k–ε* model. *Coast. Engng* **57**, 931–947.

PRICE, S.J., SUMNER, D., SMITH, J.G., LEONG, K. & PAÏDOUSSIS, M.P. 2002 Flow visualization around a circular cylinder near to a plane wall. *J. Fluids Struct.* **16**, 175–191.

RAO, A., STEWART, B.E., THOMPSON, M.C., LEWEKE, T. & HOURIGAN, K. 2011 Flows past rotating cylinders next to a wall. *J. Fluids Struct.* **27**, 668–679.

RAO, A., THOMPSON, M.C., LEWEKE, T. & HOURIGAN, K. 2013 The flow past a circular cylinder translating at different heights above a wall. *J. Fluids Struct.* **41**, 9–21.

TANIGUCHI, S. & MIYAKOSHI, K. 1990 Fluctuating fluid forces acting on a circular cylinder and interference with a plane wall. *Exp. Fluids* **9**, 197–204.

THAPA, J., ZHAO, M., ZHOU, T. & CHENG, L. 2014 Three-dimensional simulation of vortex shedding flow in the wake of a yawed circular cylinder near a plane boundary at a Reynolds number of 500. *Ocean Engng* **87**, 25–39.

WANG, X.K. & TAN, S.K. 2008 Near-wake flow characteristics of a circular cylinder close to a wall. *J. Fluids Struct.* **24**, 605–627.

WANG, R., ZHU, H., ZHOU, D., BAO, Y., PING, H., HAN, Z. & XU, H. 2020 Transition to chaos in the wake of a circular cylinder near a moving wall at low Reynolds numbers. *Phys. Fluids* **32**, 091703.

WILLIAMSON, C.H.K. 1996 Vortex dynamics in the cylinder wake. *Annu. Rev. Fluid Mech.* **28**, 477–539.

YOON, H.S., LEE, J.B., SEO, J.H. & PARK, H.S. 2010 Characteristics for flow and heat transfer around a circular cylinder near a moving wall in wide range of low Reynolds number. *Intl J. Heat Mass Transfer* **53**, 5111–5120.

ZDRAVKOVICH, M.M. 1985*a* Forces on a circular cylinder near a plane wall. *Appl. Ocean Res.* **7**, 194–201.

ZDRAVKOVICH, M.M. 1985*b* Observation of vortex shedding behind a towed circular cylinder near a wall. In *Proceedings of the 3rd International Symposium on Flow Visualization*, Ann Arbor, MI, pp. 423–427. Hemisphere.

ZDRAVKOVICH, M.M. 1997 *Flow Around Circular Cylinders, Volume 1: Fundamentals*. Oxford University Press.